Annals of Biomedical Engineering, Vol. 35, No. 8, August 2007 *(© 2007)* pp. 1368–1381
DOI: 10.1007/s10439-007-9307-9

Methods for Three-Dimensional Geometric Characterization of the Arterial Vasculature

PADRAIG M. O'FLYNN,[1,2] GERARD O'SULLIVAN,[3] and ABHAY S. PANDIT [1,2]

[1]Department of Mechanical and Biomedical Engineering, National University of Ireland, University Road, Galway, Ireland; [2]National Centre for Biomedical Engineering Science, National University of Ireland, Galway, Ireland; and [3]Section of Interventional Radiology, University College Hospital, Galway, Ireland

(Received 1 October 2006; accepted 30 March 2007; published online 13 April 2007)

Abstract—Complex vascular anatomy often affects endovascular procedural outcome. Accurate quantitative assessment of three-dimensional (3D) *in-vivo* arterial morphology is therefore vital for endovascular device design, and preoperative planning of percutaneous interventions. The aim of this work was to establish geometric parameters describing arterial branch origin, trajectory, and vessel curvature in 3D space that eliminate the errors implicit in planar measurements. 3D branching parameters at visceral and aortic bifurcation sites, as well as arterial tortuosity were determined from vessel centerlines derived from magnetic resonance angiography data for three subjects. Errors in coronal measurements of 3D branching angles for the right and left renal arteries were $3.1 \pm 3.4°$ and $7.5 \pm 3.7°$, respectively. Distortion of the anterior visceral branching angles from sagittal measurements was less pronounced. Asymmetry in branching and planarity of the common iliac arteries was observed at aortic bifurcations. The renal arteries possessed considerably greater 3D curvature than the abdominal aorta and common iliac vessels with mean average values of 0.114 ± 0.015 and 0.070 ± 0.019 mm^{-1} for the left and right, respectively. In conclusion, planar projections misrepresented branch trajectory, vessel length, and tortuosity proving the importance of 3D geometric characterization for possible applications in planning of endovascular interventional procedures and providing parameters for endovascular device design.

Keywords—Abdominal aorta, Visceral branch arteries, Common iliac arteries, Branching angle, Bifurcation planarity, Arterial tortuosity, Curvature, Torsion.

LIST OF ABBREVIATIONS AND SYMBOLS

MRA	magnetic resonance angiography
3D	three-dimensional
2D	two-dimensional
MIP	maximum intensity projection
EVAR	endovascular aneurysm repair
DICOM	digital imaging and communications in medicine
DFM	distance factor metric
κ	curvature
TC	total curvature
AC	average curvature
τ	torsion
TT	total torsion
CC	combined curvature
TCC	total combined curvature
RMS	root-mean-squared
CT	celiac trunk
SMA	superior mesenteric artery
RRA	right renal artery
LRA	left renal artery
RCIA	right common iliac artery
LCIA	left common iliac artery
COR	coronal
AX	axial
SAG	sagittal

INTRODUCTION

Arterial geometric characterization is vital to enhance our knowledge of three-dimensional (3D) vascular anatomy, particularly in regions of the arterial tree which are prone to vascular disease and subject to endovascular interventions. Although much of the early interest in measuring branching angles and branch dimensions at vascular bifurcations related to the theories of arterial geometric optimization,[21,63] most arterial characterization studies have been performed primarily to produce representative geometries for hemodynamic studies[7,17,44] or to investigate geometric features which have been implicated in the pathogenesis of atherosclerosis.[23,41] More recently

Address correspondence to Abhay S. Pandit, Department of Mechanical and Biomedical Engineering, National University of Ireland, University Road, Galway, Ireland. Electronic mail: abhay.pandit@nuigalway.ie

quantitative analyses of arterial geometries have also been performed to aid endovascular device design[19,58] and endograft sizing.[57] Hence, investigations relating to characterization of arterial branching and morphology have been focused on regions predisposed to atherosclerotic disease, in particular the aortic arch,[64] the coronary vasculature,[8,14,24] the femoral arteries,[42] and the carotid[22,44,49] and aortic[2,30,48] bifurcations. Many of these arterial characterization studies involved planar analysis of angiograms, maximum intensity projections (MIPs) from magnetic resonance angiography (MRA) or views of vascular casts for assessing 3D bifurcations and non-planar arterial curvature; methods which inevitably incur projection errors and vessel foreshortening when viewing from any direction.[59,61] Vascular cast studies are also prone to further errors due to discrepancies introduced in post-mortem preparations,[17,32] which commonly render the non-planar nature of *in-vivo* arterial bifurcations absent.[12] The combination of current 3D vascular imaging techniques and accompanying analysis software however facilitates examination of the genuine *in-vivo* 3D nature of the vasculature free from the viewing errors of 2D analysis.

Various aspects of vascular anatomy compromise endovascular device performance and complicate catheter based interventional procedures. Specifically, arterial tortuosity and branching frequently pose problems for endovascular sheath navigation, device deployment, and successful minimally invasive treatment of a particular vascular pathology. In the case of elective endovascular aneurysm repair (EVAR) alone, adverse anatomic features such as tortuosity at proximal neck and iliac fixation sites affect endograft placement and have been associated with the occurrence of endograft migration and endoleak[10,28,46] or iliac limb kinking resulting in graft thrombosis.[28,34,51,52] Difficulties in endograft sizing for complex and tortuous aneurysm morphologies often leads to the secondary placement of costly modular extensions in the common iliac arteries[56,60] or conversely inadvertent side branch occlusion,[28,29] factors which could adversely affect technical success of a procedure.

For treatment of carotid artery stenosis, severe elongation and tortuosity of the neck vessels is a major factor which precludes stenting.[1,15] Similarly, the safe delivery of embolic protection devices during percutaneous carotid interventions may be impeded by difficulty in navigating tortuous lesions[27,37] or a severely kinked distal internal carotid artery.[45] Furthermore, induced straightening of tortuous vessels during various percutaneous interventions by endovascular stents and stent-grafts occasionally precipitates complications such as vessel kinking at the stent margins.[6,39] Overly stiff device delivery systems and guidewires can cause vasospasm[11] or the occurrence of pseudolesions,[16,40,65] which inhibit angiographic assessment of the procedural outcome and often lead to unnecessary and potentially hazardous additional interventions if misdiagnosed.

A detailed knowledge of 3D access vessel morphology and deployment site geometry is therefore a major requirement in patient selection, preoperative planning, and the design of new endovascular devices for treatment of patients with a wider range of vascular anatomic variations. The goal of this study was to derive 3D geometric parameters that describe the anatomy of the normal human abdominal aorta and major peripheral branch arteries.

Specifically the aims were

1. To determine branch origin and initial trajectory of the renal and anterior visceral arteries;
2. To calculate 3D branching angles and common iliac planarity at the terminal aortic bifurcation;
3. To quantify 3D curvature, non-planarity, and overall tortuosity of the main renal arteries and infrarenal abdominal aorta and common iliac arteries; and
4. To demonstrate the magnitude of inaccuracy associated with planar analysis of 3D vascular geometry.

METHODS

Data Acquisition

Contrast-enhanced MRA scans were obtained from clinical procedures on three subjects (two men aged 47 and 64 years, and one woman aged 84 years) performed with a 1.5 T MR system (Symphony®, Siemens AG Medical Solutions, Erlangen, Germany), coronal orientation. The patients were imaged in the supine position during inspiration breath-hold. The abdominal aortic tract was imaged using 3D gadolinium-enhanced MRA. The imaging parameters for the MR acquisitions were repetition time 3.47 ms, echo time 1.42 ms, flip angle 25° slice thickness 1.5 mm. The field of view was 292.5 mm × 360 mm with matrix size 416 × 512 giving an in-plane resolution of 0.703 mm pixel^{-1}.

Segmentation and Image Analysis

Image data was segmented and visualized in a commercial processing and editing software (Mimics®, Materialise, Sheffield, UK). Once the original MRA data was loaded in DICOM (Digital Imaging and Communications in Medicine) format the orientation of the scans was specified and a coordinate system was applied automatically. A volume of interest ranging

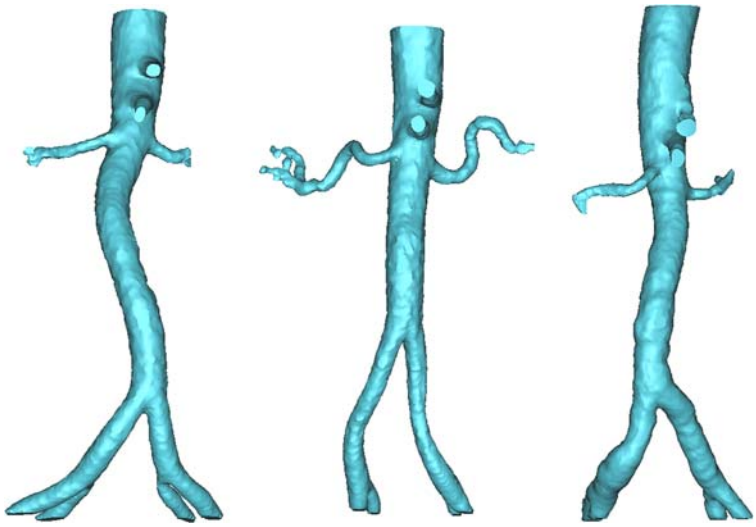

FIGURE 1. Shaded surface 3D models of the segmented abdominal aortic vasculature for the three subjects under investigation.

axially from above the celiac trunk (CT) to below the iliac bifurcations was resliced to create a project with iso-cubic voxels of dimensions 0.703 mm × 0.703 mm × 0.703 mm. Segmentation of the desired abdominal aortic vasculature was then performed by implementation of a threshold-based 3D region growing command. This segmented vascular geometry was edited to remove aortic branches and distal segments of the visceral branches which were not under investigation. Finally 3D models of the vasculature were rendered for visualization purposes as shown in Fig. 1.

The first stage in characterization of the reconstructed vascular geometry involved establishing the centerlines of the appropriate vessel segments from which the geometric parameters were calculated. The method of centerline construction involved connecting the centroids of successive two-dimensional (2D) cross-sectional lumen contours which were approximately normal to the path of the vessel. This definition of vessel centerline creation has previously been implemented using axial sections for the carotid and aortic bifurcations.[25,31,48] Individual orthogonal cross-sectional images of appropriate vessel segments were captured in Mimics® at various levels and centroid measurements obtained in image analysis software (Image Pro®, Media Cybernetics, Berkshire, UK) with an automatic threshold-based selection algorithm. The centerlines of the entire abdominal aortic tract and the common iliac arteries were established from analysis of consecutive axial sections. Slices which traversed aortic segments with irregular cross-section, such as at the transition region proximal to the aortic bifurcation (Fig. 2a) or at the level of the visceral branches (Fig. 2b), were not used for centerline determination as their centroids would be affected. The renal arteries were analyzed bilaterally from their ostia to the position of their first segmental branch while the proximal axes of the CT and the superior mesenteric artery (SMA) were established from successive coronal slices.

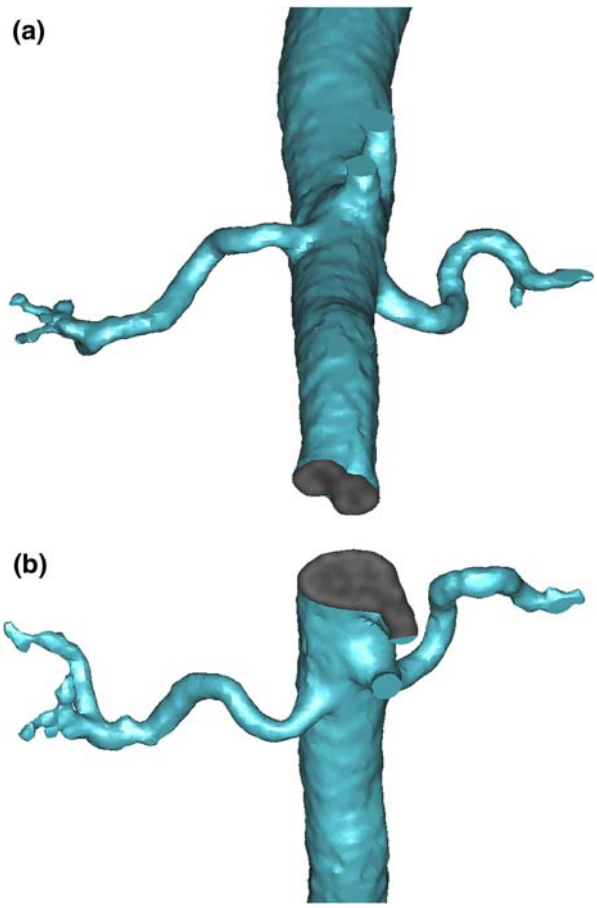

FIGURE 2. Cross sections which were disregarded during aortic centerline calculation (a) at the transition region proximal to the aortic bifurcation and (b) at the level of the visceral arteries.

Derivation of Geometrical Parameters

Branching Angles

Two different types of 3D arterial branching sites are geometrically analyzed in this study; specifically the visceral side branches and the terminal aortic bifurcation. All arterial bifurcations are typically irregular *in vivo*, parent and branch vessels are curved and their axes never intersect if extrapolated in 3D space. Despite this, arterial branching is commonly described by the angle between 2D straight line representations of the local directions of the parent and daughter vessels at the bifurcation. The straight line representations describing vessel direction adopted in previous planar geometric studies have included tangents to the arterial centerlines,[22,62] tangents to the vessel walls,[19,30,59,64] and linear least square fits of centerline points[2] in proximity to the bifurcation. Alternatively, for the few true 3D studies reported the geometric relationship between branching arterial segments has primarily been described by the angles between the directional vectors of their axes.[8,48,49,61] MRA provides 3D vascular imaging data from which these directional vectors can be derived and branching angles calculated with confidence[48,49] through an approach which alleviates the distortion encountered when measuring branching angles of 3D bifurcations from a single viewing direction.[59,61]

In the current study, centerline Cartesian coordinates of a branching vessel segment in the vicinity of the junction were represented by linear least square fits calculated using a mathematical software package (Maple®, Waterloo Maple Inc.). These best-fit lines enabled calculation of 3D vectors for parent and daughter branches which were positive in the direction of flow as represented in Figs. 3 and 5. A set number of evenly spaced centerline points, which corresponded to approximately the length of the vessel radius for the peripheral arteries, were used to determine the representative vector for each specific branch. A short vessel segment in the vicinity of the ostium was chosen to eliminate the effect of proximal branch curvature on branching angle values. Aortic vectors at individual bifurcation sites were also calculated objectively from a constant number of vessel centerline points. At the level of the visceral branches these were derived from points of the established aortic centerline directly above and below each branching level while the terminal aortic vector at the aortic bifurcation represented the segment proximal to the transition region.

Considering a parent artery represented by the directional vector **b** and a daughter branch represented by the directional vector **d**, the true angle (A) in radians between these two vectors is given by Eq. (1):

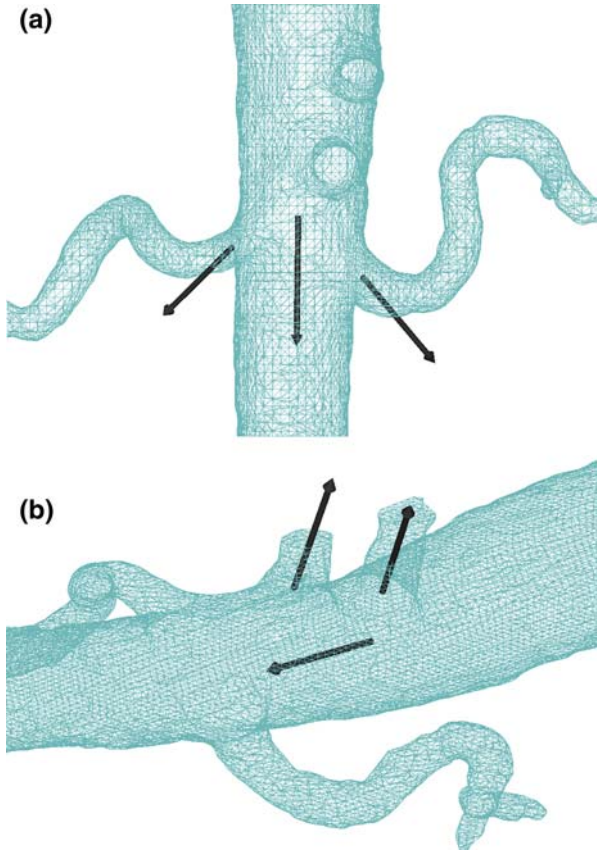

FIGURE 3. Illustration of 3D directional vectors employed for the derivation of branching angles at the visceral bifurcation sites.

$$A = \cos^{-1}\left(\frac{b \cdot d}{|b| \times |d|}\right) \tag{1}$$

Branch angles were also calculated in the principal viewing planes using this equation, in which case the directional vectors were 2D projections of the actual vessel axes onto the prescribed viewing plane. Analysis of the branch planarity at a terminal bifurcation required the computation of the acute angle between a branch artery axis and the nominal branching plane. The branching plane was determined as the best-fit plane containing the most distal point of the parent axis and the most proximal points of the daughter branch axes. The acute angle (B) that a branch directional vector **d** makes with a plane can be calculated from Eq. (2), once the principal normal vector **N** to the plane is known.

$$B = \sin^{-1}\left(\frac{N \cdot d}{|N| \times |d|}\right) \tag{2}$$

where Eq. (2) is a derivation of Eq. (1), B is in radians and the 3D normal vector **N** for a best-fit plane

obtained in Cartesian form, $Ax + By + Cz = D$, is given by (A, B, C).

Branch Angles and Origins of the Visceral Arteries

The visceral branch artery bifurcation sites are not adequately described solely by the angles defining the conventional idealized 3D bifurcations.[61] Four parameters were therefore identified to satisfactorily characterize the 3D geometry of each visceral branch site. These parameters primarily describe the location of the branch artery origin and the initial direction of the branch relative to the aorta.

The first parameter derived to portray branch direction was the 3D branching angle between the directional vector of the aorta and that of an individual visceral branch (Fig. 3), calculated using Eq. (1). The second parameter calculated, the angle of trajectory, describes the angle at which the branch emerges from the aorta when viewed in a plane perpendicular to the direction of the aortic centerline at that level. For the renal arteries this angle was calculated between the projection of the branch axis onto the orthonormal plane and the posterior aspect of the sagittal plane (Fig. 4a) while in the cases of the CT and the SMA the angle between the projection of branch axis and the left side of the median coronal plane was computed (Fig. 4b). The positions of the visceral branch origins relative to the apex of the aortic bifurcation were documented and involved calculation of the aortic centerline distance from the apex to the level of the axial mid-plane of each vessel ostium. The final parameter evaluated, the angle of origin, was an angle describing the circumferential position of the branch origin in the plane perpendicular to the centerline of the aorta at the level of that bifurcation. The angle of origin represents the angle between the anterior aspect of the median sagittal plane and a vector between the aortic centroid and the projection of the branch centerline origin onto the orthonormal plane (Fig. 4). This measure has a range 0–360° in a clockwise direction, a value of 0° signifying a branch artery emerging from the mid-anterior wall of the aorta.

Finally, branching angles for the renal and anterior visceral branches were calculated in the coronal, sagittal principal viewing planes, respectively, while angles of origin and trajectory were also determined from 2D axial projections to investigate the range of distortion errors incurred.

Aortic Bifurcation

The 3D geometry of the terminal aortic bifurcation can be characterized by angles which define the branching process into the iliac arteries and the degree of planarity at the bifurcation. The bifurcation angle θ_b was calculated as the angle between both common iliac branch axes, while the true 3D branching angles of the right and left common iliac arteries, φ_r and φ_l, respectively, were also computed as the acute angles between the 3D vectors of the terminal branches and parent artery[48] (Fig. 5). The iliac branching angles as projected on the coronal plane were calculated to determine the distortion present when measuring these angles from this viewing direction. A novel concept for quantifying planarity was employed in this study to gauge the three dimensionality of a terminal bifurcation. The planarity of each common iliac branch was determined by the angle its axis makes with the reference branching plane shown in Fig. 5 (Eq. 2). The term asymmetry is employed to describe the absolute difference of branching and planarity angles for the right and left common iliac branches.

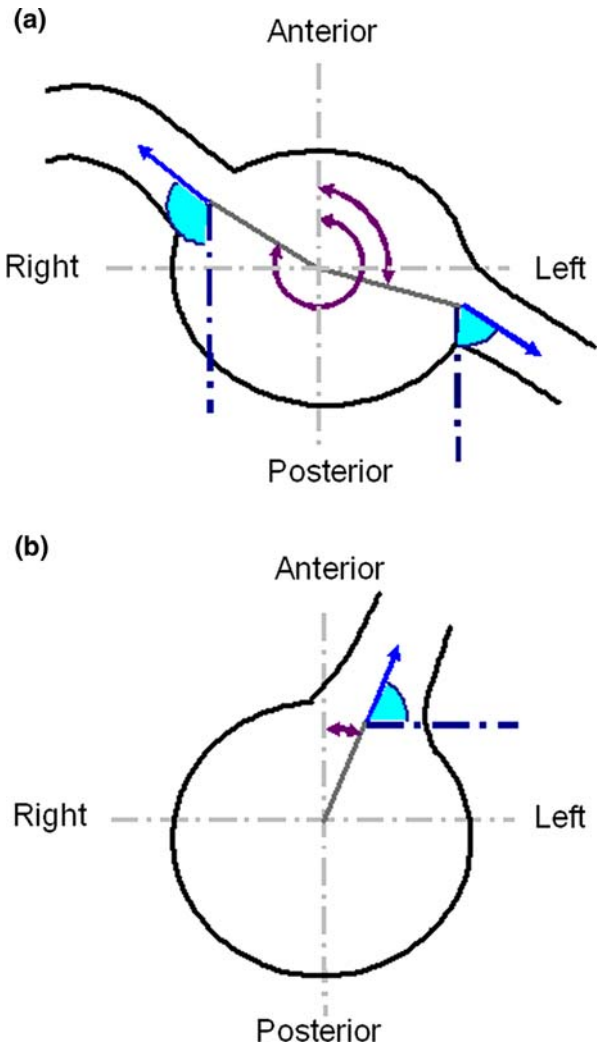

FIGURE 4. Schematic of angles of trajectory (filled) and angles of origin (arrows) for the renal arteries (a) and anterior visceral branches (b).

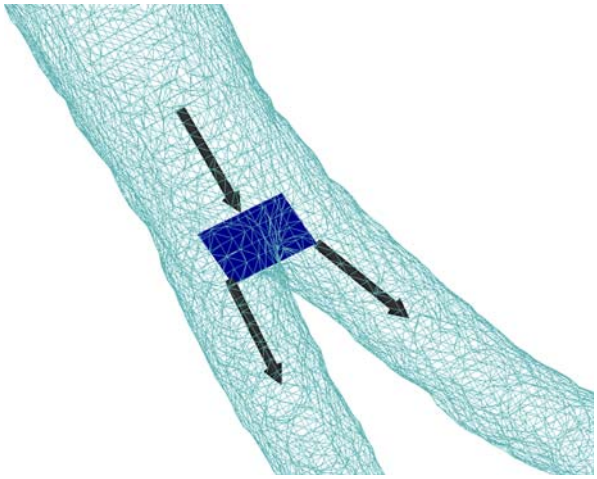

FIGURE 5. A 3D model of the aortic bifurcation displaying vessel axes, and the nominal bifurcation plane derived for calculating common iliac planarity and branching angles.

Arterial Tortuosity

Several previous investigators have quantitatively assessed *in-vivo* vessel tortuosity from planar images.[20,26,43] Actual vessel tortuosity however, will inevitably be misrepresented by 2D analysis due to projection errors because *in-vivo* arterial curvature is rarely planar and at right angles to the imaging projection. The most logical means for comprehensively describing true arterial path and quantifying tortuosity in 3D space therefore involves analysis of both vessel centerline curvature and torsion. This involves methods of analysis similar to those previously employed in investigations of coronary arterial tree configuration and dynamics.[13,18,35,38] In this study, vessel centerline curvature and torsion were calculated to describe the 3D course of aortic and peripheral vascular segments. Specifically, the *in-vivo* 3D tortuosity of the infrarenal abdominal aorta, main renal arteries, and common iliac arteries was quantified.

Distance factor metric (*DFM*). The metric employed in this work to evaluate lengthening of a vessel path due to tortuosity is simply defined by the term $L/d - 1$ where L is the length of the vessel centerline and d is the Euclidean distance between its two endpoints. This term, a derivative of the distance factor,[9,19,43] gives a dimensionless quantity which describes the amount the vessel strays from a straight line path between its endpoints with a value of zero being assigned to a straight vessel and has been reported as a reliable measure of arterial elongation in 2D[41] and 3D[8,49] studies.

Vessel curvature and torsion. Centerline coordinate data extracted from arterial segments required smoothing prior to tortuosity analysis to remove any spurious local curvature of the vessel midline which may have been present as an artefact of voxel size or the segmentation process (Fig. 6). Smoothing of the centerline data, which had an original spacing principally less than 1 mm, was achieved by fitting it with ninth-order polynomial parametric equations in terms of original arclength where arclength was determined as the length of a hermite spline curve through the initial coordinate terms. This smooth curve description was then re-sampled to give points at constant 0.2-mm intervals along the curve length. The smooth centerline data was subsequently re-fitted with a similar order polynomial curve, in parametric form as a function of arclength (s) of the revised points. These fitted curves needed to be three times differentiable to provide the closed form solutions of derivatives along the arterial path required for curvature and torsion calculations. All curve fitting was performed in Matlab® to obtain parameterized centerline curves for each arterial segment (Fig. 7), in the form, $r(s) = (x(s), y(s), z(s))$ where $R^2 > 0.99$ for all fits.

Curvature at a discrete point along a space curve $r(s)$ is defined as the reciprocal of the radius of the osculating circle, where the center of the osculating circle lies on the normal vector of the Frenet frame and the osculating plane is defined by the normal and tangent vector to the curve at that point (Fig. 8). In

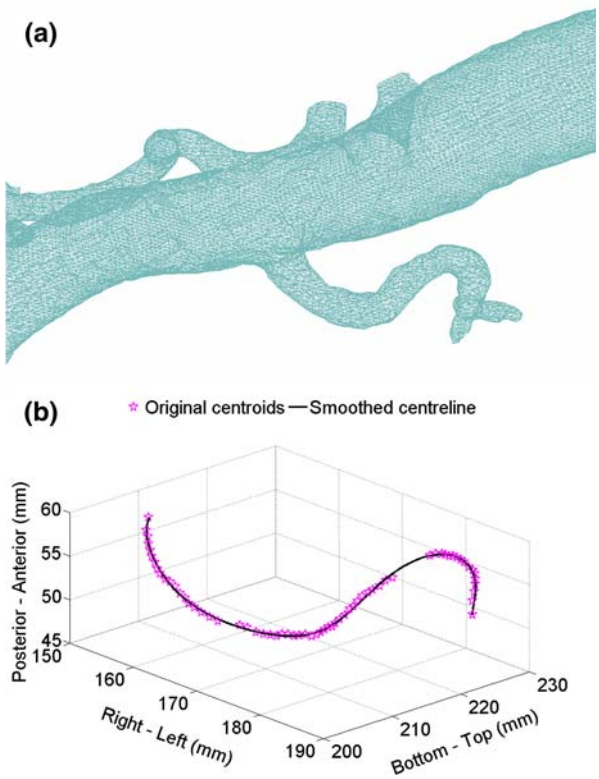

FIGURE 6. Depiction of the smoothed vessel centerline of the left renal artery determined from extracted centroids.

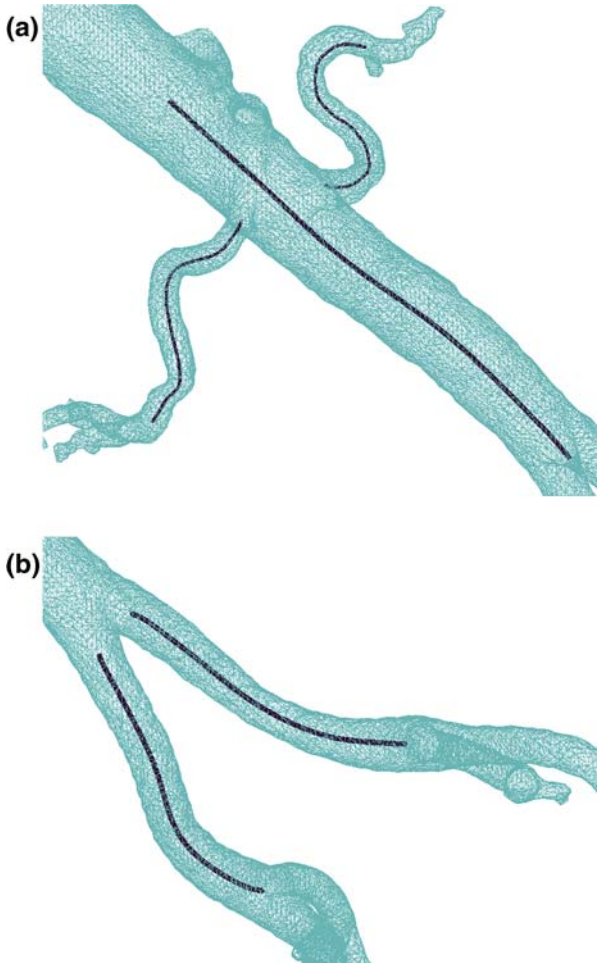

FIGURE 7. Wireframe model of the *in-vivo* (a) infrarenal abdominal aorta and its left and right renal branches and (b) common iliac arteries with spline representations of the smoothed centerlines.

this study curvature (κ) was calculated using a standard formula from the Frenet–Serret theory of differential geometry (Eq. 3):

$$\kappa = \frac{|\mathbf{r}'(s) \times \mathbf{r}''(s)|}{[\mathbf{r}'(s)]^3} \tag{3}$$

where $\mathbf{r}'(s)$ and $\mathbf{r}''(s)$ are the first and second derivatives of the centerline curve and $|\mathbf{r}'(s) \times \mathbf{r}''(s)|$ is the magnitude of their cross-product. This formula is altered for analysis of 2D curvature as displayed in Eq. (4) for the principal x–y orthogonal plane. Planar curvature can be positive or negative and a change in sign of this expression denotes an inflection point:

$$\kappa_{2D} = \frac{x'(s)y''(s) - y'(s)x''(s)}{[x'(s)^2 + y'(s)^2]^{3/2}} \tag{4}$$

The non-planar nature of 3D vessel curvature was gauged by a measure of torsion of its centerline. Torsion describes the rate of change in orientation of the

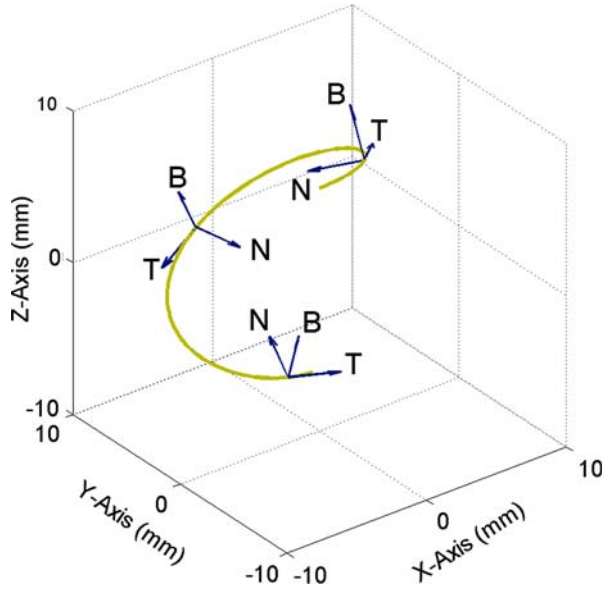

FIGURE 8. 3D spiraling curve of non-uniform curvature and torsion illustrating rotation of the Frenet frame along its length. The Frenet frame consists of three orthogonal vectors: the *normal vector* N and *tangent vector* T define the osculating plane while the unit *binormal vector* B completes the triad. Change in orientation of B indicates torsion of the curve.

osculating plane along a space curve. Again for a vessel centerline, torsion (τ) was calculated from a derivative relation by means of differential geometric principles related to the Frenet–Serret formulae (Eq. 5):

$$\tau = \frac{[\mathbf{r}'(s), \mathbf{r}''(s), \mathbf{r}'''(s)]}{|\mathbf{r}'(s) \times \mathbf{r}''(s)|^2} \tag{5}$$

where $\mathbf{r}'''(s)$ is the third derivative of the curve and $[\mathbf{r}'(s), \mathbf{r}''(s), \mathbf{r}'''(s)]$ denotes a scalar triple product. All derivatives of the smooth-fitted centerline curves essential for obtaining curvature and torsion values were calculated in Matlab®. Torsion is positive for a right-handed curve and negative for a left-handed curve. If torsion equals zero, then a curve is planar.

Finally the term combined curvature (CC) was assigned to a property which accounts for curvature and torsion at an individual point, and is calculated according to Eq. (6):

$$CC = \sqrt{\kappa^2 + \tau^2} \tag{6}$$

Curvature, torsion, and combined curvature were calculated at a number (n) of evenly spaced points along the centerline generating an array of measurements at constant increments of arclength. A sampling frequency (ω) of 5 points/mm was employed throughout this study giving measurements at 0.2-mm intervals. These ordered sets of values were then utilized to

calculate reliable total and average measures of the defining parameters as demonstrated for curvature in Eqs. (7) and (8), respectively.

$$TC = \sum_{i=1}^{n} |\kappa_i| \tag{7}$$

$$AC = \frac{\sum_{i=1}^{n} |\kappa_i|}{n} \tag{8}$$

Accuracy Assessment of Length, Curvature, and Torsion Determination

The method of data smoothing and curve fitting employed to analyze arterial centerline length, curvature, and torsion was validated by comparing calculated values with analytically determined values for standard simulated curves. A sequence of points at a specific constant spacing along the generated curve served as the input data for the current method of analysis, with three-point spacing intervals investigated for each curve (0.5, 1, and 1.5 mm). Three circular curves of different radii (r), described in parametric form by $x = r \times \cos(t)$; $y = r \times \sin(t)$; $t = 0$–2π, were utilized to analyze the accuracy of planar curvature calculations. The true curvature of a circle is known to be uniform along its circumference and is given by $\kappa = 1/r$ allowing radii to be chosen for these simulated curves which corresponded to curvature values within the physiological range for arteries.

In order to investigate accuracy of 3D curvature, torsion, and combined curvature calculations, three helical curves of various defining parameters were generated and analyzed (Fig. 9). Coils are a set of space curves for which curvature and torsion are uniform along their length and therefore allowed easy comparison of experimental calculations with the theoretical values derived from the following formulas:

$$\kappa = \frac{R}{R^2 + c^2} \tag{9}$$

$$\tau = \frac{c}{R^2 + c^2} \tag{10}$$

$$CC = \sqrt{\frac{1}{R^2 + c^2}} \tag{11}$$

A standard helix can be described in parametric form, $x = R \times \cos(t)$; $y = R \times \sin(t)$; $z = c \times t$, by a coil radius (R) and a frequency parameter (c) which controls the axial separation of the helical loops given by $2 \times \pi \times c$. Once more the specific helical space curves examined were chosen to represent variations within the physiological range of curvature and torsion shown by *in-vivo* arterial vessels.[14,66]

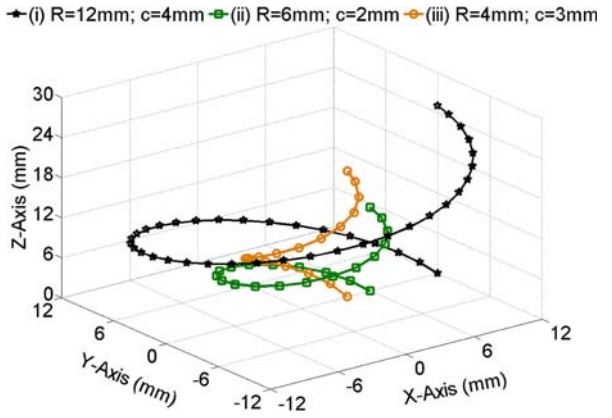

FIGURE 9. Helical curves generated to assess accuracy of curvature and torsion calculations with the following properties: (i) $L = 79.5$ mm, $\kappa = 0.075$ mm^{-1}, $\tau = 0.025$ mm^{-1}; (ii) $L = 39.7$ mm, $\kappa = 0.15$ mm^{-1}, $\tau = 0.05$ mm^{-1}; and (iii) $L = 31.4$ mm, $\kappa = 0.16$ mm^{-1}, $\tau = 0.12$ mm^{-1}.

Errors in length were less than 0.15 mm in all cases for both 2D and 3D test curves. The error for curvature, torsion, or combined curvature at a point was estimated as the absolute difference between the theoretical and calculated values and was compiled as a percentage of the theoretical value, the root-mean-square (RMS) of which is reported for entire curves at the prescribed sampling frequency (ω) of 5 points/mm. RMS errors in curvature for the 2D circular test curves with different original data point spacing were all less than 0.69%. RMS errors in curvature, torsion, and combined curvature for the simulated helical curves were also very small with values less than 0.66, 1.76, and 0.61% for each parameter, respectively. Maximum errors in calculated parameters were consistently observed at the extremities of both 2D and 3D curves and reached no greater than seven times the RMS error value in any case. Predominantly lower RMS and maximum error values were observed for 2D and space curves when the original data points were closely spaced and more numerous. Overall, this analysis revealed accuracy in measurement of curve length and a robust method of planar curvature and 3D curvature and torsion analysis.

In-Vivo Vessel Tortuosity

3D centerlines of the main renal arteries and common iliac branches were analyzed to quantify the distance factor metric, 3D curvature, its non-planarity and the resultant magnitude of combined curvature. Similar measures of 3D tortuosity were evaluated for the infrarenal abdominal aorta ranging from below the lowest renal branch extending to a level in the terminal

aorta proximal to the transition region. In order to avoid maximum errors in curve fitting affecting any *in-vivo* measurements however, calculated curvature, torsion, and combined curvature for the most proximal and distal 3 mm of each centerline were not reported. Planar tortuosity analysis was carried out for each arterial segment in appropriate principal orthogonal views to assess the magnitude of distortion encountered in length, curvature, and elongation. 2D measurements were calculated in coronal and axial projections for the renal vessels while lateral and antero-posterior curvature was characterized for the infrarenal abdominal aorta and common iliac vessels in the coronal and sagittal planes.

RESULTS

Branch Angles and Origins of the Visceral Arteries

Geometric parameters describing the initial trajectory and ostial positions of the anterior visceral branches and the renal arteries are presented in Table 1 for three subjects. Mean 3D branching angles for the right and left renal arteries were $55.9 \pm 7.2°$ and $62.6 \pm 2.4°$. Those for the CT and SMA were similar but showed greater variability. The right renal artery (RRA) emerged more anteriorly than the left renal artery (LRA) as demonstrated by the angle of trajectory and angle of origin values which corresponds to its course around the vena cava. Angles of origin and trajectory for the CT and SMA show that the ostial location and initial direction of these branches was in general more to the left than perfectly anterior. Of interest, spacing of the CT-SMA and SMA-RRA branch mid-levels relative to each other as determined by the aortic centerline distances was consistent for the subjects analyzed with values of 15.9 ± 0.8 and 13.9 ± 1.6 mm, respectively. The LRA arose lower than the RRA although only marginally in one case.

Renal artery branching angles as observed in the coronal plane were calculated as $54.5 \pm 5.3°$ and $55.1 \pm 4.6°$ for the right and left, respectively, corresponding to errors of $3.1 \pm 3.4°$ and $7.5 \pm 3.7°$ when compared to the actual 3D angles. Distortion errors of the anterior visceral branching angles from sagittal measurements were less pronounced. Angles of origin showed little distortion when determined in the axial transverse plane; however axial angles of trajectory exhibited significant errors with maximum values up to 13.5°.

Aortic Bifurcation

Geometric parameters for the aortic bifurcation analyzed included a 3D bifurcation angle (θ_b) of $43.4 \pm 9.0°$, and right and left common iliac branching angles, φ_r and φ_l, of $29.1 \pm 11.4°$ and $14.3 \pm 5.4°$. 2D analysis of the aortic bifurcation site for these subjects in the coronal plane was associated with projection errors of 0.9 ± 1.1 and $32.9 \pm 19.3\%$ for the branching angles of the right and left common iliac arteries, respectively, and miscalculation of the bifurcation angle by $5.1 \pm 3.1\%$. The planarity angles recorded between the common iliac arteries and the nominal plane of the bifurcation were $6.7 \pm 2.8°$ and $7.4 \pm 4.4°$ for the right and left branches specifically. Noticeable asymmetry in branching and planarity of the common iliac arteries was present at the aortic bifurcations with mean values of $7.4 \pm 8.9°$ and $4.1 \pm 3.1°$ observed.

In-Vivo Vessel Tortuosity

Results from quantitative 3D tortuosity analysis of various *in-vivo* arterial segments for three subjects are summarized in Table 2. Mean average curvature for the renal arteries were 0.114 ± 0.015 and 0.070 ± 0.019 mm^{-1} for the left and right, respectively. Although the RRA was predominantly longer than the left both set of arteries displayed similar levels of total curvature. 3D curvature of the LRA possessed greater non-planarity than that of the right as demonstrated by mean average torsion values, and consequently returned a larger mean average combined curvature measurement. The abdominal aorta (AA), right common iliac artery (RCIA), and left common iliac artery (LCIA) exhibited significantly less total and average curvature than the renal arteries, but still showed

TABLE 1. Geometric parameters describing the major visceral bifurcations.

	Aortic C_L distance (mm)	3D branching Angle (°)	Angle of trajectory (°)	Angle of origin (°)	Error in planar branching angle (°)	Error in axial angle of trajectory (°)	Error in axial angle of origin (°)
CT	142.1 ± 19.8	56.0 ± 24.0	75.3 ± 20.7	30.6 ± 4.9	2.6 ± 1.9	4.3 ± 5.7	1.0 ± 0.8
SMA	126.2 ± 19.2	62.9 ± 18.2	73.6 ± 22.1	14.4 ± 5.6	1.9 ± 1.6	5.6 ± 6.9	1.1 ± 1.4
RRA	112.2 ± 17.8	55.9 ± 7.2	123.7 ± 19.3	301.1 ± 6.2	3.1 ± 3.4	4.0 ± 3.7	0.5 ± 0.7
LRA	106.0 ± 19.0	62.6 ± 2.4	59.2 ± 11.1	111.9 ± 5.0	7.5 ± 3.7	6.9 ± 4.9	1.0 ± 1.5

TABLE 2. Measures of 3D *in-vivo* arterial tortuosity.

	L (mm)	*DFM*	*TC* (mm^{-1})	*AC* (mm^{-1})	*TT* (mm^{-1})	*AT* (mm^{-1})	*TCC* (mm^{-1})	*ACC* (mm^{-1})
LRA	31.8 ± 24.4	0.263 ± 0.294	13.62 ± 11.28	0.114 ± 0.015	35.46 ± 18.06	0.527 ± 0.406	42.26 ± 14.49	0.569 ± 0.389
RRA	42.7 ± 18.2	0.168 ± 0.120	13.95 ± 10.49	0.070 ± 0.019	35.67 ± 12.41	0.203 ± 0.028	42.16 ± 18.58	0.233 ± 0.012
AA	96.6 ± 19.9	0.036 ± 0.017	6.40 ± 2.34	0.014 ± 0.003	47.18 ± 11.36	0.111 ± 0.054	49.21 ± 10.48	0.116 ± 0.053
LCIA	50.6 ± 22.8	0.012 ± 0.011	4.36 ± 0.96	0.022 ± 0.008	56.51 ± 15.76	0.305 ± 0.157	57.34 ± 15.56	0.308 ± 0.155
RCIA	53.4 ± 22.5	0.050 ± 0.044	6.71 ± 3.51	0.029 ± 0.012	43.95 ± 11.02	0.237 ± 0.173	45.68 ± 10.24	0.244 ± 0.170

considerable torsion which resulted in only minimal elongation of their vessel centerlines.

Longitudinal profiles of 3D curvature, torsion, and combined curvature as generated for the LRA of a single subject in Fig. 10 provide a complete representation of the varying severity of curvature, non-planarity, and overall tortuosity along the length of the artery which may not be conveyed by the summary measures in Table 2. These profiles show the complex nature of the arterial paths which boast non-uniform curvature and torsion, and relate peaks in curvature or torsion to positions along the length of the artery. A comparison of longitudinal curvature and torsion for the arterial segments analyzed in the same subject is also afforded by Fig. 11.

The errors in results for 2D curvature determined from the renal, aortic, and common iliac arterial segments as calculated in appropriate principal viewing planes are reported in Table 3. In general, the total and average values for curvature observed from planar projections of the 3D vessel centerlines poorly represent the actual arterial curvature that was obtained from 3D analysis. Errors in planar average curvature can be attributed to distortion of the centerline path in a particular viewing direction. Percentage errors in total curvature were generally greater than those for average curvature due to the additional effects of the vessel's foreshortened appearance.

Of interest, the significant errors in planar total and average curvature values present in both orthogonal planes for the arterial vessels analyzed demonstrate the 3D nature of the *in-vivo* vessel curvature. Although errors in arterial length from planar measurements were greatest for the renal arteries, noticeable foreshortening was also detected for both common iliac artery branches in the coronal and sagittal planes.

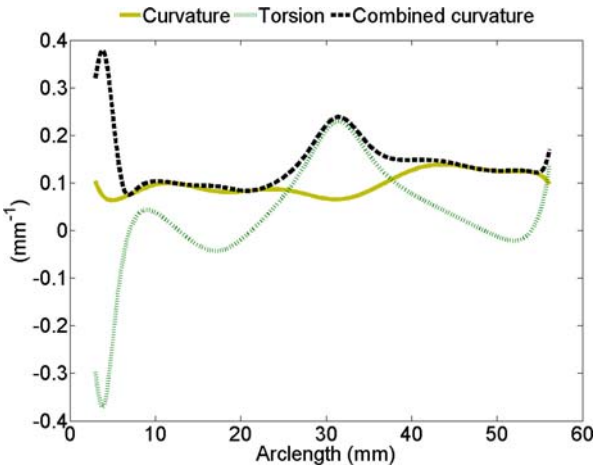

FIGURE 10. Plot of centerline curvature, torsion, and resultant combined curvature vs. arterial length for the left renal artery depicted in Fig. 6.

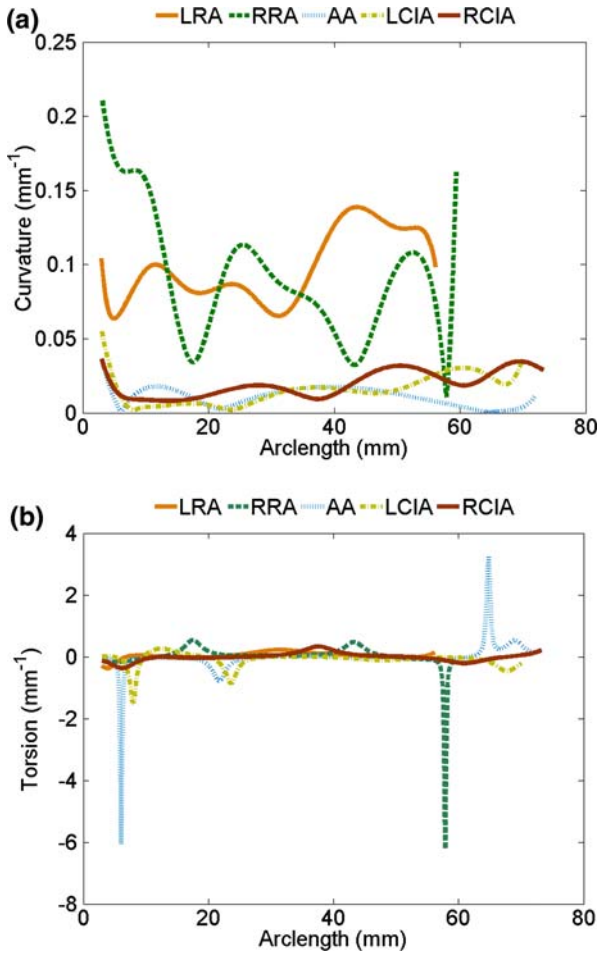

FIGURE 11. Comparative plots of (a) curvature and (b) torsion vs. longitudinal position for all analyzed *in-vivo* arterial segments shown in Fig. 7.

TABLE 3. Errors associated with planar measurement of arterial length and tortuosity.

	Plane	*L* (mm)	Foreshortening (%)	Error in *DFM* (%)	Error in planar *TC* (%)	Error in planar *AC* (%)
LRA	COR	29.3 ± 22.2	6.8 ± 1.8	21.9 ± 20.1	17.3 ± 13.4	9.1 ± 14.4
	AX	24.2 ± 14.5	17.5 ± 13.7	69.4 ± 24.9	48.0 ± 23.9	66.3 ± 28.0
RRA	COR	37.8 ± 15.0	10.5 ± 4.0	57.1 ± 19.1	28.7 ± 15.3	20.9 ± 15.5
	AX	37.4 ± 13.5	10.9 ± 5.6	36.2 ± 18.7	31.3 ± 12.7	23.3 ± 11.0
AA	COR	93.9 ± 18.6	2.7 ± 0.9	63.4 ± 29.6	39.0 ± 26.4	37.1 ± 27.9
	SAG	94.7 ± 18.4	1.8 ± 1.5	35.7 ± 27.8	31.6 ± 20.8	30.5 ± 19.9
LCIA	COR	46.2 ± 21.9	9.3 ± 2.3	30.8 ± 14.1	22.4 ± 3.0	13.1 ± 3.0
	SAG	46.9 ± 22.2	7.1 ± 7.0	45.5 ± 22.3	41.1 ± 4.0	35.2 ± 10.0
RCIA	COR	46.5 ± 21.1	12.9 ± 9.8	67.5 ± 37.0	39.5 ± 15.1	29.1 ± 14.9
	SAG	49.6 ± 22.8	8.5 ± 6.6	34.9 ± 27.0	24.2 ± 11.3	16.9 ± 14.8

DISCUSSION

Vessel geometry can affect endovascular device performance and plays a crucial role in the technical success of various interventional procedures. In this study a strategy has been presented which enables *in-vivo* assessment of the 3D configuration of arterial flow channels. Until recently true 3D arterial geometric characterization studies have posed substantial methodological difficulties due to the complex, non-planar configuration of arterial vessels. An approach which utilizes the true volumetric nature of MRA imaging data for geometric analysis, as described in this study, enables derivation of geometric parameters to comprehensively describe branch origin and trajectory and arterial tortuosity in 3D space which eliminate the inaccuracies implicit with planar measurements.

Although some errors exist associated with the reconstruction of vascular geometries from MRI,[32,33] the resolution of the image data employed in this study provided the adequate pixel/radius ratios required for accurate segmentation[32] of the vessels analyzed. All arterial centerlines were also determined directly from 2D segmented slices and do not include the additional inaccuracies introduced by 3D surface generation.[47] Arterial reconstructions from MR imaging have previously been deemed suitable for quantitative geometric characterization studies of the peripheral vasculature and the reliability and reproducibility of derived branching angle parameters has been demonstrated.[48,49] While segmentation of the arterial geometry was achieved in this study with a semi-automatic 3D region growing command, the method of vessel centerline identification involved a series of operator-dependent tasks, a fact which may limit its application to a large number of clinical cases. Accuracy of the method was maintained however by minimizing the manual procedures and employing threshold based algorithms for lumen cross-section selection during image analysis. Thus removing the effects of operator variability and giving a higher level of control on centroid measurement. The method described enabled a robust centerline length, curvature, and torsion calculation once point data was fitted with polynomial functions in parametric form for smoothing as revealed by results of the accuracy assessment.

The branching angles reported in this study for the visceral arteries are within the range of those previously reported from the 2D analysis of angiograms,[21] cadavers,[36] and MIPs from MRA.[19] Similarly the angles of origin and trajectory obtained from orthonormal planes transecting the visceral bifurcation sites correspond well with similar angles reported in the literature derived from axial transverse CT[5,54] and MRA projections.[19] As observed from the results of this study the branching angles and angles of trajectory are prone to distortion from projection errors associated with 2D measurements. This is due to the fact that the orientation of the branch axis relative to the viewing plane can greatly influence its projection onto that plane and consequently its perceived direction in space. The geometric parameters derived in this work which eliminate projection errors and describe in detail the 3D visceral bifurcation sites could specifically aid more accurate design and customization of fenestrated and branched endografts for treatment of juxtarenal abdominal aortic aneurysms.

A novel definition for describing terminal branching planarity is proposed in this study and complements the branching parameters previously evaluated by Sun *et al.*[48] to completely describe the 3D nature of branching at the aortic bifurcation. Former quantification of aortic bifurcation planarity worked under the assumption that iliac branch axes were coplanar,[25] which is rarely the scenario *in vivo* as verified here by asymmetry of planarity angles for the right and left common iliac arteries. 3D geometric parameters describing branching and non-planarity of the aortic bifurcation could prove important to iliac limb design for bifurcated endografts, and if adapted to generic terminal bifurcations may well assist the design of bifurcated stent systems.

Although 3D elongation measurements of the renal arteries similar to those observed in this study have previously been reported[19] no comparable studies have been conducted regarding in-depth 3D analysis of abdominal aortic or peripheral arterial tortuosity. The ranges of arterial curvature and torsion obtained in this study are similar however to physiological values reported for 3D reconstructions of the coronary arteries generated from biplane angiography.[14,18,38,66] Experimental results of *in-vivo* arterial tortuosity portrayed non-uniformity of vessel curvature and torsion over the artery length. Although physiological arterial curvature was observed to vary continuously within quite a tight range for the vessels studied (Fig. 11a) torsion was subject to greater fluctuations. Of interest torsion values alternated from positive to negative corresponding to vessel segments with differing directions of twist. Large peaks in torsion were observed at positions with sudden changes in orientation of the plane of curvature (Fig. 11b). Comparison of results from planar curvature or length calculations with actual 3D data demonstrated the inadequacy of 2D measurements in the presence of any significant 3D tortuosity. Vessel foreshortening in 2D projection images occurs due to the inability to visualize the extent of non-planar arterial curvature or even due to out-of-plane angulation of a relatively straight vessel. The observed foreshortening in principal orthogonal views of the infrarenal aorta and common iliac arteries, for the current subjects although noticeable is only mild compared to that which is encountered when analyzing the tortuous vasculature routinely present in elderly patients with aortic aneurysms. Subsequently the limitations of planar length measurements due to projection errors which diminish apparent length of an artery have been well documented in relation to planning EVAR.[3,4] Numerous investigations into the 3D measurement of aorto-iliac length have therefore been conducted recently to improve sizing of endograft prostheses[50,53,57] and reduce the incidence of unnecessary exclusion of the internal iliac arteries or alternatively the need for placement of iliac limb extensions.

Quantification of 3D physiological vessel tortuosity by the robust methods described in this work may provide valuable information for improving stent and endograft limb flexibility and conformability in curved peripheral arteries. The methods outlined could be extended to assess how stent deployment in tortuous arteries impacts on vessel geometry or to reliably determine peripheral vessel dynamics due to respiration[19] and limb movement.[55] Alternatively the proposed 3D measures of tortuosity provide a possible means for quantitatively assessing the viability of vascular access routes for endovascular device delivery during preoperative planning.

In summary the parameters derived for 3D geometric characterization of the arterial vasculature overcome the limitations of planar analysis and may aid the standardization of 3D geometric definitions. The methods of vascular quantification may also provide essential data to facilitate future device development for endovascular treatment of vascular disease, particularly in cases of complex anatomy.

CONCLUSION

Anatomic features such as vessel branching and tortuosity often impact on percutaneous interventional outcome and endovascular device performance. Patient-specific *in-vivo* quantification of these features may assist decision making during interventions and aid device sizing and customization. The purpose of this study was to develop objective methods for analyzing 3D *in-vivo* peripheral arterial geometry derived from MR angiographic data. Geometric parameters were derived to describe genuine 3D branching morphology and a method for determination of peripheral arterial curvature and torsion is proposed. Specifically the origin and initial trajectory of the major visceral branches relative to the aorta were documented and parameters describing the non-planar asymmetrical nature of the aortic bifurcation were calculated. Centerline curvature, torsion, and combined curvature for the main renal arteries, infrarenal abdominal aorta, and common iliac vessels were quantified to describe 3D arterial tortuosity. The errors associated with conventional planar geometric measurements from standard angiographic planes were assessed for the subjects analyzed. This investigation confirmed that 3D methods are required for any meaningful and realistic analysis of *in-vivo* arterial tortuosity due to the non-planar configuration of the vasculature. Similarly planar branching angles and angles of trajectory were subject to considerable projection errors. In conclusion the geometric parameters derived in this work allow accurate *in-vivo* quantification of 3D arterial vessel geometry which may aid in planning of endovascular interventional procedures, and in realistic modeling of arterial geometries for improving endovascular device design.

ACKNOWLEDGMENTS

The authors would like to acknowledge Ms. Geraldine Dowd, Clinical Specialist Radiographer, University College Hospital, Galway for her help and James Coburn for his technical expertise. This work was supported with

funds from Irish Research Council for Science, Engineering, and Technology (IRCSET): funded by the National Development Plan.

REFERENCES

[1]Ahmadi, R. A., M. Schillinger, M. Haumer, A. Willfort, and E. Minar. Carotid stenting in a case of combined kinking and stenosis. *Cardiovasc. Intervent. Radiol.* 24:197–199, 2001.

[2]Bargeron, C. B., G. M. Hutchins, G. W. Moore, O. J. Deters, F. F. Mark, and M. H. Friedman. Distribution of the geometric parameters of human aortic bifurcations. *Arteriosclerosis* 6:109–113, 1986.

[3]Beebe, H. G. Imaging modalities for aortic endografting. *J. Endovasc. Surg.* 4:111–123, 1997.

[4]Beebe, H. G., T. Jackson, and J. P. Pigott. Aortic aneurysm morphology for planning endovascular aortic grafts: limitations of conventional imaging methods. *J. Endovasc. Surg.* 2:139–148, 1995.

[5]Beregi, J. P., B. Mauroy, S. Willoteaux, C. Mounier-Vehier, M. Remy-Jardin, and J. Francke. Anatomic variation in the origin of the main renal arteries: spiral CTA evaluation. *Eur. Radiol.* 9:1330–1334, 1999.

[6]Berkefeld, J., B. Turowski, A. Dietz, H. Lanfermann, M. Sitzer, T. Schmitz-Rixen, H. Steinmetz, and F. E. Zanella. Recanalization results after carotid stent placement. *Am. J. Neuroradiol.* 23:113–120, 2002.

[7]Bharadvaj, B. K., R. F. Mabon, and D. P. Giddens. Steady flow in a model of the human carotid bifurcation. Part I. Flow visualization. *J. Biomech.* 15:349–362, 1982.

[8]Brinkman, A. M., P. B. Baker, W. P. Newman, R. Vigorito, and M. H. Friedman. Variability of human coronary artery geometry: an angiographic study of the left anterior descending arteries of 30 autopsy hearts. *Ann. Biomed. Eng.* 22:34–44, 1994.

[9]Bullitt, E., G. Gerig, S. M. Pizer, W. L. Lin, and S. R. Aylward. Measuring tortuosity of the intracerebral vasculature from MRA images. *IEEE Trans. Med. Imaging* 22:1163–1171, 2003.

[10]Buth, J., and R. J. Laheij. Early complications and endoleaks after endovascular abdominal aortic aneurysm repair: report of a multicenter study. *J. Vasc. Surg.* 31:134–146, 2000.

[11]Cardaioli, P., M. Giordan, M. Panfili, and R. Chioin. Complication with an embolic protection device during carotid angioplasty. *Catheter. Cardiovasc. Intervent.* 62:234–236, 2004.

[12]Caro, C. G., D. J. Doorly, M. Tarnawski, K. T. Scott, Q. Long, and C. L. Dumoulin. Non-planar curvature and branching of arteries and non-planar-type flow. *Proc. R. Soc. London* 452:185–197, 1996.

[13]Chen, S. Y., and J. D. Carroll. Kinematic and deformation analysis of 4-D coronary arterial trees reconstructed from cine angiograms. *IEEE Trans. Med. Imaging* 22:710–721, 2003.

[14]Chen, S. Y. J., J. D. Carroll, and J. C. Messenger. Quantitative analysis of reconstructed 3-D coronary arterial tree and intracoronary devices. *IEEE Trans. Med. Imaging* 21:724–740, 2002.

[15]Chong, P. L., K. Salhiyyah, and P. D. Dodd. The role of carotid endarterectomy in the endovascular era. *Eur. J. Vasc. Endovasc. Surg.* 29:597–600, 2005.

[16]Dawson, D. L., J. C. Hellinger, T. T. Terramani, S. Najibi, L. G. Martin, and A. B. Lumsden. Iliac artery kinking with endovascular therapies: technical considerations. *J. Vasc. Interv. Radiol.* 13:729–733, 2002.

[17]Ding, Z., K. Wang, J. Li, and X. Cong. Flow field and oscillatory shear stress in a tuning-fork-shaped model of the average human carotid bifurcation. *J. Biomech.* 34:1555–1562, 2001.

[18]Ding, Z., H. Zhu, and M. H. Friedman. Coronary artery dynamics *in vivo*. *Ann. Biomed. Eng.* 30:419–429, 2002.

[19]Draney, M. T., C. K. Zarins, and C. A. Taylor. Three-dimensional analysis of renal artery bending motion during respiration. *J. Endovasc. Ther.* 12:380–386, 2005.

[20]Eze, C. U., R. Gupta, and D. L. Newman. A comparison of quantitative measures of arterial tortuosity using sine wave simulations and 3D wire models. *Phys. Med. Biol.* 45:2593–2599, 2000.

[21]Fanucci, E., A. Orlacchio, and M. Pocek. The vascular geometry of human arterial bifurcations. *Invest. Radiol.* 23:713–718, 1988.

[22]Forster, F. K., P. M. Chikos, and J. S. Frazier. Geometric modeling of the carotid bifurcation in humans: implications in ultrasonic Doppler and radiologic investigations. *J. Clin. Ultrasound* 13:385–390, 1985.

[23]Friedman, M. H., O. J. Deters, F. F. Mark, C. B. Bargeron, and G. M. Hutchins. Arterial geometry affects hemodynamics. A potential risk factor for athersoclerosis. *Atherosclerosis* 46:225–231, 1983.

[24]Friedman, M. H., and Z. Ding. Relation between the structural asymmetry of coronary branch vessels and the angle at their origin. *J. Biomech.* 31:273–278, 1998.

[25]Friedman, M. H., and Z. Ding. Variability of the planarity of the human aortic bifurcation. *Med. Eng. Phys.* 20:469–472, 1998.

[26]Hart, W. E., M. Goldbaum, B. Cote, P. Kube, and M. R. Nelson. Measurement and classification of retinal vascular tortuosity. *Int. J. Med. Inform.* 53:239–252, 1999.

[27]Henry, M., I. Henry, C. Klonaris, I. Masson, M. Hugel, K. Tzvetanov, G. Ethevenot, B. E. Le, S. Kownator, F. Luizi, and B. Folliguet. Benefits of cerebral protection during carotid stenting with the PercuSurge GuardWire system: midterm results. *J. Endovasc. Ther.* 9:1–13, 2002.

[28]Kalliafas, S., J. N. Albertini, J. Macierewicz, S. W. Yusuf, S. C. Whitaker, S. T. Macsweeney, P. W. Wenham, and B. R. Hopkinson. Incidence and treatment of intraoperative technical problems during endovascular repair of complex abdominal aortic aneurysms. *J. Vasc. Surg.* 31:1185–1192, 2000.

[29]Lee, W. A., Y. G. Wolf, B. B. Hill, P. Cipriano, T. J. Fogarty, and C. K. Zarins. The first 150 endovascular AAA repairs at a single institution: how steep is the learning curve? *J. Endovasc. Ther.* 9:269–276, 2002.

[30]Lee, Y. T., W. F. Keitzer, F. R. Watson, and H. Liu. Vascular geometry at the abdominal aortic bifurcation. *J. Am. Med. Womens Assoc.* 37:77–81, 1982.

[31]Long, Q., X. Y. Xu, M. Bourne, and T. M. Griffith. Numerical study of blood flow in an anatomically realistic aorto-iliac bifurcation generated from MRI data. *Magn. Reson. Med.* 43:565–576, 2000.

[32]Moore, J. A., B. K. Rutt, S. J. Karlik, K. Yin, and C. R. Ethier. Computational blood flow modeling based on in vivo measurements. *Ann. Biomed. Eng.* 27:627–640, 1999.

[33]Moore, J. A., D. A. Steinman, and C. R. Ethier. Computational blood flow modelling: errors associated with

reconstructing finite element models from magnetic resonance images. *J. Biomech.* 31:179–184, 1998.
[34]Naslund, T. C., W. H. Edwards Jr, D. F. Neuzil, R. S. Martin III, S O. Snyder Jr, J. L. Mulherin Jr, M. Failor, and K. McPherson. Technical complications of endovascular abdominal aortic aneurysm repair. *J. Vasc. Surg.* 26:502–509, discussion 509–510, 1997.
[35]Pao, Y. C., J. T. Lu, and E. L. Ritman. Bending and twisting of an in vivo coronary artery at a bifurcation. *J. Biomech.* 25:287–295, 1992.
[36]Pennington, N., and R. W. Soames. The anterior visceral branches of the abdominal aorta and their relationship to the renal arteries. *Surg. Radiol. Anat.* 27:395–403, 2005.
[37]Powell, R. J., C. Alessi, B. Nolan, E. Rzucidlo, M. Fillinger, D. Walsh, M. Wyers, R. Zwolak, and J. L. Cronenwett. Comparison of embolization protection device-specific technical difficulties during carotid artery stenting. *J. Vasc. Surg.* 44:56–61, 2006.
[38]Puentes, J., C. Roux, M. Garreau, and J. L. Coatrieux. Dynamic feature extraction of coronary artery motion using DSA image sequences. *IEEE Trans. Med. Imaging* 17:857–871, 1998.
[39]Quinn, S. F., J. Kim, R. C. Sheley, and J. H. Frankhouse. "Accordion" deformity of a tortuous external iliac artery after stent-graft placement. *J. Endovasc. Ther.* 8:93–98, 2001.
[40]Sharma, S., and R. M. Makkar. Percutaneous intervention on the LIMA: tackling the tortuosity. *J. Invasive Cardiol.* 15:359–362, 2003.
[41]Smedby, O. Geometrical risk factors for atherosclerosis in the femoral artery: a longitudinal angiographic study. *Ann. Biomed. Eng.* 26:391–397, 1998.
[42]Smedby, O., and L. Bergstrand. Tortuosity and atherosclerosis in the femoral artery: what is cause and what is effect? *Ann. Biomed. Eng.* 24:474–480, 1996.
[43]Smedby, O., N. Hogman, S. Nilsson, U. Erikson, A. G. Olsson, and G. Walldius. 2-Dimensional tortuosity of the superficial femoral-artery in early atherosclerosis. *J. Vasc. Res.* 30:181–191, 1993.
[44]Smith, R. F., B. K. Rutt, A. J. Fox, R. N. Rankin, and D. W. Holdsworth. Geometric characterization of stenosed human carotid arteries. *Acad. Radiol.* 3:898–911, 1996.
[45]Spanos, V., G. Stankovic, and A. Colombo. A tortuous distal carotid artery: how to overcome the problem, with the aim of guaranteeing distal protection. *Int. J. Cardiovasc. Intervent.* 5:77–80, 2003.
[46]Stanley, B. M., J. B. Semmens, Q. Mai, M. A. Goodman, D. E. Hartley, C. Wilkinson, and M. D. Lawrence-Brown. Evaluation of patient selection guidelines for endoluminal AAA repair with the Zenith Stent-Graft: the Australasian experience. *J. Endovasc. Ther.* 8:457–464, 2001.
[47]Steinman, D. A., J. B. Thomas, H. M. Ladak, J. S. Milner, B. K. Rutt, and J. D. Spence. Reconstruction of carotid bifurcation hemodynamics and wall thickness using computational fluid dynamics and MRI. *Magn. Reson. Med.* 47:149–159, 2002.
[48]Sun, H., B. D. Kuban, P. Schmalbrock, and M. H. Friedman. Measurement of the geometric parameters of the aortic bifurcation from magnetic resonance images. *Ann. Biomed. Eng.* 22:229–239, 1994.
[49]Thomas, J. B., L. Antiga, S. L. Che, J. S. Milner, D. A. Steinman, J. D. Spence, and B. K. Rutt. Variation in the carotid bifurcation geometry of young versus older adults: implications for geometric risk of atherosclerosis. *Stroke* 36:2450–2456, 2005.
[50]Tillich, M., B. B. Hill, D. S. Paik, K. Petz, S. Napel, C. K. Zarins, and G. D. Rubin. Prediction of aortoiliac stent-graft length: comparison of measurement methods. *Radiology* 220:475–483, 2001.
[51]Torsello, G., N. Osada, H. J. Florek, S. Horsch, H. Kortmann, G. Luska, R. Scharrer-Pamler, W. Schmiedt, T. Umscheid, and G. Wozniak. Long-term outcome after Talent endograft implantation for aneurysms of the abdominal aorta: a multicenter retrospective study. *J. Vasc. Surg.* 43:277–284, 2006.
[52]Umscheid, T., and W. J. Stelter. Time-related alterations in shape, position, and structure of self-expanding, modular aortic stent-grafts: a 4-year single-center follow-up. *J. Endovasc. Surg.* 6:17–32, 1999.
[53]Velazquez, O. C., E. Y. Woo, J. P. Carpenter, M. A. Golden, C. F. Barker, and R. M. Fairman. Decreased use of iliac extensions and reduced graft junctions with software-assisted centerline measurements in selection of endograft components for endovascular aneurysm repair. *J. Vasc. Surg.* 40:222–227, 2004.
[54]Verschuyl, E. J., R. Kaatee, F. J. Beek, G. Pasterkamp, W. H. Bush, J. J. Beutler, P. J. van der Ven, and W. P. Mali. Renal artery origins: location and distribution in the transverse plane at CT. *Radiology* 203:71–75, 1997.
[55]Wensing, P. J., F. G. Scholten, P. C. Buijs, M. J. Hartkamp, W. P. Mali, and B. Hillen. Arterial tortuosity in the femoropopliteal region during knee flexion: a magnetic resonance angiographic study. *J. Anat.* 187(Pt 1):133–139, 1995.
[56]White, G. H., J. May, R. Waugh, J. P. Harris, X. Chaufour, W. Yu, and M. S. Stephen. Shortening of endografts during deployment in endovascular AAA repair. *J. Endovasc. Surg.* 6:4–10, 1999.
[57]Whittaker, D. R., J. Dwyer, and M. F. Fillinger. Prediction of altered endograft path during endovascular abdominal aortic aneurysm repair with the Gore Excluder. *J. Vasc. Surg.* 41:575–583, 2005.
[58]Wijesinghe, L. D., D. J. Scott, and D. Kessel. Analysis of renal artery geometry may assist in the design of new stents for endovascular aortic aneurysm repair. *Br. J. Surg.* 84:797–799, 1997.
[59]Willems, P. W., K. S. Han, and B. Hillen. Evaluation by solid vascular casts of arterial geometric optimisation and the influence of ageing. *J. Anat.* 196:161–171, 2000.
[60]Wolf, Y. G., M. Tillich, W. A. Lee, G. D. Rubin, T. J. Fogarty, and C. K. Zarins. Impact of aortoiliac tortuosity on endovascular repair of abdominal aortic aneurysms: evaluation of 3D computer-based assessment. *J. Vasc. Surg.* 34:594–599, 2001.
[61]Zamir, M. Three-dimensional aspects of arterial branching. *J. Theor. Biol.* 90:457–476, 1981.
[62]Zamir, M., and N. Brown. Arterial branching in various parts of the cardiovascular system. *Am. J. Anat.* 163:295–307, 1982.
[63]Zamir, M., and N. Brown. Internal geometry of arterial bifurcations. *J. Biomech.* 16:857–863, 1983.
[64]Zamir, M., and P. Sinclair. Origin of the brachiocephalic trunk, left carotid, and left subclavian arteries from the arch of the human aorta. *Invest. Radiol.* 26:128–133, 1991.
[65]Zanchetta, M., L. Pedon, G. Rigatelli, Z. Olivari, M. Zennaro, and P. Maiolino. Pseudo-lesion of internal mammary artery graft and left anterior descending artery during percutaneous transluminal angioplasty—a case report. *Angiology* 55:459–462, 2004.
[66]Zhu, H., and M. H. Friedman. Relationship between the dynamic geometry and wall thickness of a human coronary artery. *Arterioscler. Thromb. Vasc. Biol.* 23:2260–2265, 2003.